Journal of
Materials Chemistry C

Materials for optical, magnetic and electronic devices

Accepted Manuscript

This article can be cited before page numbers have been issued, to do this please use: C. Cuerva, J. A. Campo, M. Cano and R. Schmidt, *J. Mater. Chem. C*, 2019, DOI: 10.1039/C9TC03627J.

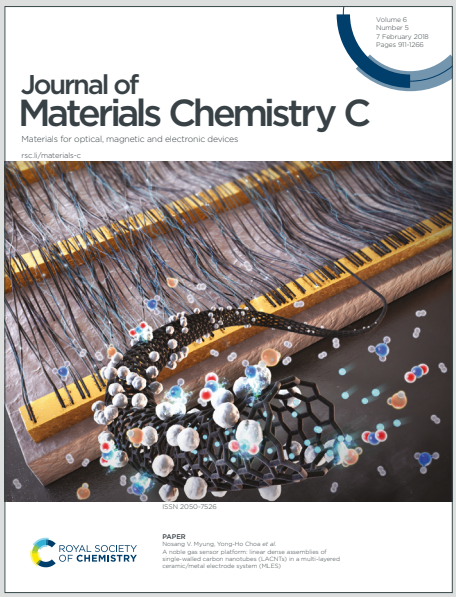

ROYAL SOCIETY OF CHEMISTRY

rsc.li/materials-c

View Article Online
DOI: 10.1039/C9TC03627J

ARTICLE

Lamellar columnar liquid-crystalline mesophases as a 2D platform for anhydrous proton conduction

Received 00th January 20xx,
Accepted 00th January 20xx

DOI: 10.1039/x0xx00000x

Cristián Cuerva,*[a,b] José A. Campo, [a] Mercedes Cano*[a] and Rainer Schmidt[c]

Several series of dihalide Pd(II) compounds bearing pyridyl or isoquinolinylpyrazole ligands have been strategically designed and synthesised to exhibit columnar mesomorphism in wide stability ranges. The coordination of the pyrazoles to the fragments PdX_2 (X = Cl, Br, I) generates half-disc molecules that are capable to be self-assembled in discotic dimers via intermolecular interactions. This disc-like shape is required for the supramolecular organisation of the lamellar columnar mesophases, which are formed at temperatures below 100 ºC in most cases. It was found that these metallomesogens behave as 2D proton conducting materials upon anhydrous conditions. The high fluidity properties of the mesophase facilitates proton conduction as a result of the spontaneous dissociation of the acidic pyrazole proton at the melting temperature. For the first time, lamellar columnar mesophases are demonstrated to serve as a 2D platform to induce water-free proton conductivity in dihalide Pd(II) metallomesogens.

Introduction

The development of proton exchange membrane (PEM) fuel cells as an alternative to gasoline and diesel engines constitutes one of the most active research lines in the field of clean energy. At present, the fabrication of PEM fuel cells with fast start up, high power density, long operation times and low operation temperatures is already a reality.[1] Furthermore, highly-compact PEM fuel cells with low corrosion effects have been successfully developed looking for their implementation in portable devices and vehicles.[2] However, several factors mainly related to the cost and durability of this technology are slowing down its final commercialisation.[3] Novel electrolytes are required to develop efficient PEM fuel cells that can operate in wide ranges of temperature, upon anhydrous conditions, and during successive cycles without degradation of the material.[4]

Highly-ordered materials with cavities or channels where ions can move with a certain degree of freedom are being investigated nowadays. Many systems based on metal-organic frameworks,[5] perovskites,[6] mesoporous silicas[7] and self-assembled molecules[8] have been shown to be useful for fast ionic conduction, although humid conditions are generally required for enhancing proton conductivity. In this context, liquid crystals can be considered as advantageous materials for this purpose due to their ability to combine the two key factors for efficient ionic conduction: crystalline order to form nanochannels for ion transport and fluidity to enhance ion mobilities.[9] Liquid-crystalline mesophases consist of molecules exhibiting long-range order, but still they show similar fluidity properties than those found in the isotropic liquid state. Both factors are of great interest because they allow operating under anhydrous conditions and give access to wide temperature ranges.[10] It should be noted that the type of the molecular assembly is a determinant feature since the channels can be opened through different space directions, and ion-conduction can be one-dimensional (columnar mesophase),[9a, 11] two-dimensional (smectic mesophases)[12] or three-dimensional (bicontinuous cubic mesophases).[13] A common strategy used to obtain ion-conductive liquid crystals is designing ionic salts in which the different counterions can act as charge carriers. Thus, several ionic liquid crystals containing imidazolium, pyridinium, tetrafluoroborate and hexafluorophosphate counterions, among others, have been shown to exhibit one-, two-, or three-dimensional ionic conduction in the mesophase.[12,14] Also, purely organic molecules or coordination compounds that are functionalised with terminal acidic groups have been considered.[9a] Deprotonation in the mesophase is possible and the proton jump between neighbouring molecules may be favoured by the cooperative motions of molecules, which may generate fast proton conduction.

In a previous work, we have reported on a family of dichloride pyridylpyrazole Pd(II) metallomesogens $[PdCl_2(Hpz^{R(n,n)py})]$ that exhibit lamellar columnar (Col_L)

[a] Department of Inorganic Chemistry, Complutense University of Madrid, Ciudad Universitaria, 28040 Madrid, Spain. Email: mmcano@ucm.es
[b] BIOSCOPE Research Group, LAQV@REQUIMTE, Chemistry Department, Faculty of Science and Technology, NOVA University Lisbon, 2829-516 Caparica, Portugal. Email: c.alaiz@fct.unl.pt
[c] GFMC, Department of Materials Physics, Faculty of Physics, Complutense University of Madrid, Ciudad Universitaria, 28040 Madrid, Spain.

†Electronic Supplementary Information (ESI) available: structural characterisation of all the Pd(II) compounds, selected bond distances and angles for **9**·CH_3CN and **19**, DSC thermogram for **10**, bar diagram showing the range of existence of solid and liquid crystal phases for all the Pd(II) compounds, and Z'' vs. Z' plots for **27** in the isotropic liquid phase. CCDC 1937943-1937944. For ESI and crystallographic data in CIF or other electronic format see DOI: 10.1039/x0xx00000x

View Article Online
DOI: 10.1039/C9TC03627J

Table 1 Numbering of the dihalide Pd(II) metallomesogens

Compound	Type	n	Number
[$PdCl_2(Hpz^{R(n,n)py})$][a]	**I**	4	**1**
		6	**2**
		8	**3**
		10	**4**
		12	**5**
		14	**6**
		16	**7**
		18	**8**
[$PdBr_2(Hpz^{R(n,n)py})$]		6	**9**
		12	**10**
		14	**11**
		16	**12**
		18	**13**
[$PdI_2(Hpz^{R(n,n)py})$]		6	**14**
		12	**15**
		14	**16**
		16	**17**
		18	**18**
[$PdCl_2(Hpz^{R(n,n)iq})$]	**II**	4	**19**
		6	**20**
		8	**21**
		10	**22**
		12	**23**
		14	**24**
		16	**25**
		18	**26**
[$PdBr_2(Hpz^{R(n,n)iq})$]		12	**27**
		14	**28**
		16	**29**
		18	**30**
[$PdI_2(Hpz^{R(n,n)iq})$]		12	**31**
		14	**32**
		16	**33**
		18	**34**

The dichloride Pd(II) compounds [$PdCl_2(Hpz^{R(n,n)py})$] **1**-**8** were reported previously by us.[15]

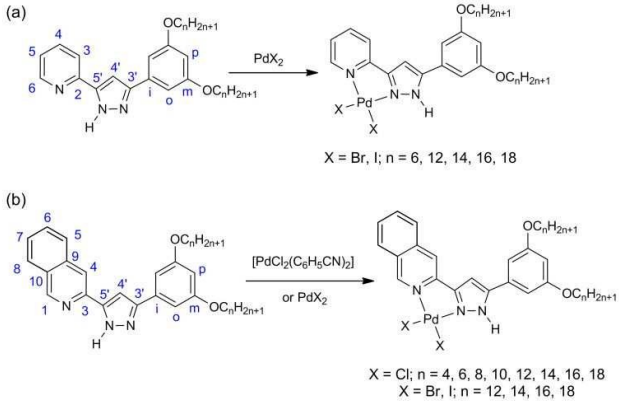

Scheme 1 Synthesis procedure to dihalide Pd(II) compounds (a) [$PdX_2(Hpz^{R(n,n)py})$] and (b) [$PdX_2(Hpz^{R(n,n)iq})$]. Solvents and conditions: CH_2Cl_2, reflux, 24 h. The atom numbering used for NMR assignment is also indicated. For more synthetic details, see the Experimental Section.

mesophases (compounds **1**-**8** in Table 1).[15] Their supramolecular organisation involves the formation of columns into a lamellar lattice, which is not usually found in liquid crystal materials and only some few species of this type have been reported in the literature.[16] It is shown here that they provide a suitable platform for two-dimensional proton conduction which has not been reported before from the best of our knowledge. Encouraged to explore the dielectric behaviour of these systems, we have now synthesised new series of dihalide pyridylpyrazole Pd(II) metallomesogens [$PdX_2(Hpz^{R(n,n)py})$] (X = Br, I) with the final goal of improving both the thermal stability and the mesomorphic behaviour of those systems (compounds **9**-**18** in Table 1). In addition, the pyrazole ligand was strategically designed to have an isoquinoline substituent on the basis of consider that an increase in the conjugation should contribute to a decrease of the melting temperatures and a high stabilisation of the lamellar columnar (Col_L) mesophases over larger temperature ranges. Thus, the new compounds [$PdX_2(Hpz^{R(n,n)iq})$] (X = Cl, Br, I) (compounds **19**-**34** in Table 1) were obtained. In the present work, we report the synthesis, characterisation and thermal behaviour of the new dihalide Pd(II) metallomesogens as well as the dielectric properties and conductivity of all compounds to demonstrate their potential application as electrolytes in fuel cells. A schematic representation of the studied compounds is drawn in Scheme 1.

RESULTS AND DISCUSSION

Synthesis and structural characterisation

The synthesis and characterisation of the dihalide pyridylpyrazole Pd(II) compounds [$PdX_2(Hpz^{R(n,n)py})$] **1**-**8** (type **I**) were reported previously by us.[15] The new dihalide Pd(II) compounds [$PdX_2(Hpz^{R(n,n)py})$] **9**-**18** (type **I**) and [$PdX_2(Hpz^{R(n,n)iq})$] (type **II**) **19**-**34** were synthesised by reaction of the corresponding pyrazoles [$Hpz^{R(n,n)py}$] or [$Hpz^{R(n,n)iq}$] with bis(benzonitrile)dichloridepalladium(II) or with metal salts PdX_2 (X = Br, I) in a 1 : 1 (ligand : metal) molar ratio. Scheme 1 shows the synthetic route followed including the required reagents and conditions. The compounds were isolated in yields greater than 50% in the form of solids that are stable at room temperature. All compounds were fully characterised by IR and NMR spectroscopies and elemental analysis (see Experimental Section and ESI†). IR and ^{1}H NMR spectra show the expected signals of the pyrazole, benzene and pyridine or isoquinoline fragments. It is noteworthy that the typical signal attributed to the NH group is present in both the solid-state IR spectra and in the ^{1}H NMR ones. In fact, the four-bond coupling between this NH proton and the H4' proton of the pyrazole *core* was detected in the ^{1}H NMR spectra of these species, because the H4' signal generally appears as a doublet with a coupling constant of 1 - 2 Hz. To confirm this fact, selective irradiation of the NH proton was made at *ca.* 10.6 ppm. As a result, the signal of the H4' proton was observed as a singlet due to decoupling from the NH group.

View Article Online
DOI: 10.1039/C9TC03627J

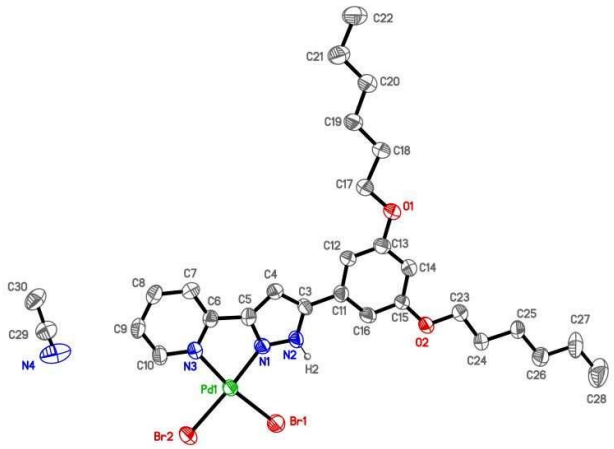

Figure 1 ORTEP plot for $[PdBr_2(Hpz^{R(6,6)py})]\cdot CH_3CN$, **9**·$CH_3CN$, with 40% probability. Hydrogen atoms, except H2, have been omitted for clarity.

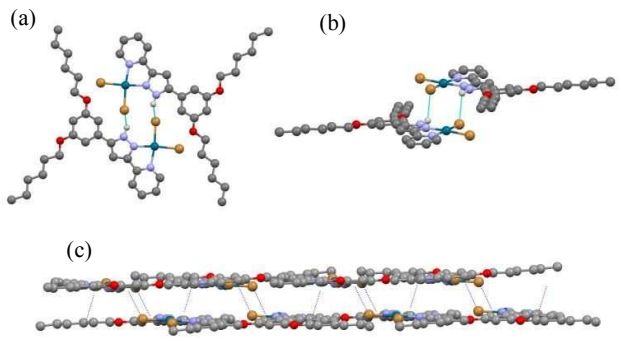

Figure 2 (a, b) Dimers generated by weak N–H···Br hydrogen bonds. Hydrogen atoms, except H2, have been omitted for clarity. (c) Double layer in the *bc* plane (contacts: blue N···Br; purple: C···C between chains). Contacts in the layer C···O are omitted.

Additional ^1H-^1H COSY and selective 1D NOESY NMR spectra were required in order to assign all resonances. DEPT and 2D ^1H–^{13}C HMQC and ^1H–^{13}C HMBC NMR experiments were also carried out to obtain the correct interpretation of the ^{13}C NMR spectra. All the spectroscopic data are given in detail as ESI†.

Single crystals suitable for X-ray diffraction experiments were also obtained for **9** (type **I**) and **19** (type **II**). This allowed studying the individual structure and the stacking of molecules in the crystal for both types of compounds.

Crystal structure of $[PdBr_2(Hpz^{R(6,6)py})]\cdot CH_3CN$, 9·$CH_3CN$

Single crystals of **9**·CH_3CN suitable for X-ray studies were grown from a dichloromethane/acetonitrile solution (3:1 %v/v) of **9**, by slow evaporation of the solvents. Acetonitrile was used as the poor-solvent to favour the nucleation of compound **9**, which crystallises in the monoclinic system (space group C2/c) with a molecule of CH_3CN. The molecular structure is depicted in Figure 1 and Table S1 lists selected bond distances and angles.

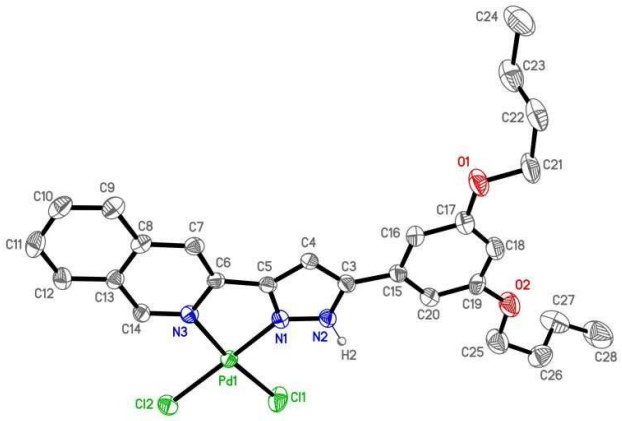

Figure 3 ORTEP plot for $[PdCl_2(Hpz^{R(4,4)iq})]$ **19** with 30% probability. Hydrogen atoms, except H2, have been omitted for clarity.

The metal centre is four-coordinated in a square-planar geometry, bonded to two bromide ligands and one nitrogen atom of the pyrazole core and the nitrogen atom of the pyridine group of the pyridylpyrazole ligand acting in a bidentate fashion (Figure 1). As a consequence of this coordination, the major deviation of the ideal square-planar geometry is shown in the N3–Pd–N1 bite angle of 79.3(1)º (Table S1). The Pd–N and Pd–Br distances were found to be *ca.* 2.0 and 2.4 Å, respectively, with a Br2–Pd–Br1 bond angle of 92.5(1)º (Table S1).

A five-membered metallocycle defined by the atoms Pd1N1C5C6N3 is generated as a result of the bidentate coordination of the pyridylpyrazole to the palladium metal centre. This metallocycle is almost coplanar with the Pd1N1N3Br2Br1 coordination plane, exhibiting a dihedral angle of 3.2(2)º. The dihedral angle between the pyridine plane and the own pyrazole is 2.2(2)º, which indicates that both rings are situated in approximately the same plane. By contrast, the benzene substituent is slightly twisted with respect to the pyrazole one, as deduced from the dihedral angle of 8.0(2)º. The terminal alkyl chains are fully extended in the same plane than that defined by the benzene group (torsion angles of *ca.* 175–178º), and they are also almost coplanar with the benzene ring. Note that the angles between the line that connects the extremes of each chain and the normal vector to the benzene plane are found to be 88.1(2) and 90.0(2)º.

As shown in Figure 2a, molecules interact with the neighbouring ones through weak N–H···Br hydrogen bonds (d(N2···Br1): 3.460(5) Å, ∠(N2–H2···Br1): 124.7º, symmetry operation: 1-*x*, 1-*y*, 1-*z*). The dibromide Pd(II) molecules exhibit a half-disc molecular shape, which give rise to head-to-tail dimers with a disc-like shape through the mentioned hydrogen bonds. In this situation, the palladium centres have a distance of 6.83(1) Å between each other (Figure 2b).

The molecular stacking of compound **9** can be represented by double layers of chains in the *bc* plane. The head-to-tail dimers are connected by non-conventional C···O hydrogen bonds (d(C9···O2): 3.395(1) Å, ∠(C9–H9···O2): 170.2º,

View Article Online
DOI: 10.1039/C9TC03627J

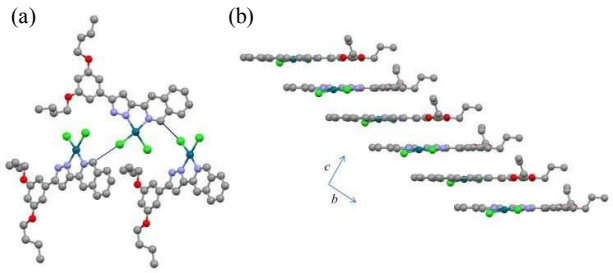

Figure 4 (a) Detail of the C···Cl hydrogen bonds involving twisted molecules of [$PdCl_2(Hpz^{R(4,4)iq})$] **19**. (b) View of one of the columns through the *a* axis.

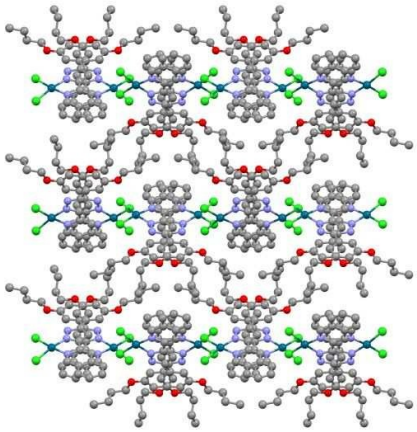

Figure 5 Columnar packing of [$PdCl_2(Hpz^{R(4,4)iq})$] **19** driven by C···Cl hydrogen bonds and π···π interactions.

symmetry operation: *x*, 1-*y*, *z*-½) and weak interactions between chains (Figure 2c).

Crystal structure of [$PdCl_2(Hpz^{R(4,4)iq})$] 19

X-ray single crystals of **19** were obtained by a slow evaporation of a chloroform solution of this compound. In this case, the compound **19** crystallises in the orthorhombic system, space group Pbca. The molecular structure is depicted in Figure 3 and selected bond lengths and angles are given in Table S2.

The coordination mode is similar to that of the analogous dibromide Pd(II) compound **9** above described. The metal centre is bonded to two nitrogen atoms, one of the pyrazole core and the other from the isoquinoline group, and the two chloride atoms, thus generating a square-planar environment with Pd–N and Pd–Cl distances of *ca.* 2.02 and 2.28 Å, respectively (Table S2). The bidentate coordination of the isoquinolinylpyrazole ligand generates a slight deviation of the ideal square-planar geometry, showing a N1–Pd–N3 bite angle of 79.7(2)º. The metallocycle defined by the PdN1C5C6N3 atoms is almost coplanar with the PdN1N3Cl1Cl2 coordination plane (dihedral angle of 4.5(1)º). Likewise, the isoquinoline moiety and the benzene ring are also coplanar with the own pyrazole ring (dihedral angles of 0.3(1)º and 3.1(1)º, respectively). Only the terminal alkyl chains show a major deviation with respect to the benzene group because they

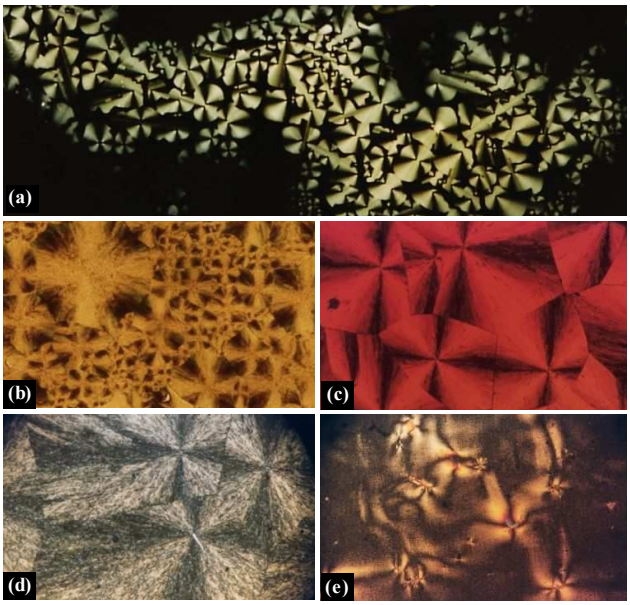

Figure 6 POM microphotographs of the mesophase of (a) [$PdCl_2(Hpz^{R(16,16)iq})$] **25** at 132 ºC, (b) [$PdBr_2(Hpz^{R(18,18)py})$] **13** at 99 ºC, (c) [$PdI_2(Hpz^{R(12,12)py})$] **15** at 110 ºC, (d) [$PdBr_2(Hpz^{R(14,14)iq})$] **28** at 173 ºC, and (e) [$PdI_2(Hpz^{R(18,18)iq})$] **34** at 149 ºC. All images were taken on cooling under crossed polarisers

point out of the molecular core in an orthogonal direction (Figure 3). The angles between the normal vector to the benzene plane and the line that connects the extremes of each chain are found to be of 55.5(1)º and 73.8(1)º. Therefore, the whole molecule can be considered to be approximately planar, with the exception of the peripherical chains.

Each molecule interacts with two neighbours through weak C···Cl hydrogen bonds (d(C14 ··· Cl1) = 3.40(1) Å; ∠(C14–H14···Cl1): 127.8º; symmetry operations: *x*, *y* - ½, -*z* + ½; *x*, *y* + ½, -*z* + ½) (Figure 4a). However, the interacting molecules are not in the same plane, they are twisted 73º (measured as the dihedral angle between the metallocycle planes). The shortest Pd···Pd distance of 6.4(1) Å is found between these unities. Also, a very weak interaction between the Cl2 ligand and the nitrogen atom of the same neighbouring molecule is observed (d(N2···Cl2) = 3.62(1) Å; ∠(N2–H2···Cl2): 141.6º; symmetry operations: *x*, *y* - ½, -*z* + ½; *x*, *y* + ½, -*z* + ½).

Weak π···π lateral interactions involving both the pyrazole and the isoquinoline rings of neighbouring molecules are established, so generating columns along the *b*-axis with a ladder distribution (Figure 4b). Therefore, the supramolecular packing can be defined as a lamellar-columnar organisation with a layer distribution driven by weak interactions (hydrogen bonds and π···π interactions) in which the chloride atoms and the aromatic rings are involved (Figure 5).

Mesomorphic behaviour

The mesomorphic properties of the dichloride Pd(II) metallomesogens [$PdCl_2(Hpz^{R(n,n)py})$] **1**-**8** (type **I)** had already been investigated previously by us.[15] Here in this work, polarised light optical microscopy (POM) studies revealed that

View Article Online
DOI: 10.1039/C9TC03627J

Table 2 Thermal behaviour of dibromide and diiodide pyridylpyrazole Pd(II) compounds [$PdBr_2(Hpz^{R(n,n)py})$] **9**-**13** and [$PdI_2(Hpz^{R(n,n)py})$] **14**-**18**

n		Transition[a]	T[b] [ºC] (ΔH [kJ mol^{-1}])	n		Transition[a]	T[b] [ºC] (ΔH [kJ mol^{-1}])
Compounds [$PdBr_2(Hpz^{R(n,n)py}$)]				*Compounds [$PdI_2(Hpz^{R(n,n)py}$)]*			
6	**9**	Cr→I	230 (28.8)	6	**14**	Cr→I	195 (31.6)
		I→Cr	203 (-25.2)			I→Cr	141 (-24.9)
12	**10**	Cr→Cr'→Col_L→I	80 (4.8), 89 (24.6), 167 (14.1)	12	**15**	Cr→Cr'→Col_L→I	59 (10.3), 91 (17.6), 157 (24.6)
		I→Col_L→Cr	142 (-14.7), 79 (-19.5)			I→Col_L→Cr	130 (-23.2), 79 (-12.9)
14	**11**	Cr→Col_L→I	95 (31.5), 176 (18.3)	14	**16**	Cr→Cr'→Col_L→I	52 (10.6), 91 (24.8), 153 (24.2)
		I→Col_L→Cr	147 (-16.5), 87 (-28.4)			I→Col_L→Cr	128 (-21.5), 90 (-19.1)
16	**12**	Cr→Col_L→I	103 (44.5), 174 (23.6)	16	**17**	Cr→Cr'→Col_L→I	56 (6.5), 103 (29.6), 146 (18.8)
		I→Col_L→Cr	149 (-19.4), 92 (-18.6)			I→Col_L→Cr	143[c], 93 (-15.8)
18	**13**	Cr→Cr'→Col_L→I	81 (4.7), 105 (46.9), 159 (15.8)	18	**18**	Cr→Col_L→I	108 (39.7), 147 (20.4)
		I→Col_L→Cr	133 (-10.7), 94 (-36.1)			I→Col_L→Cr	139[c], 91[c]

[a] Cr, Cr' = crystalline phases, Col_L = lamellar columnar mesophase, I = isotropic liquid. [b] DSC onset peaks. [c] Detected by POM.

Table 3 Thermal behaviour of dihalide isoquinolinylpyrazole Pd(II) compounds **19**-**34**

n		Transition[a]	T[b] [ºC] (ΔH [kJ mol^{-1}])	n		Transition[a]	T[b] [ºC] (ΔH [kJ mol^{-1}])
Compounds [$PdCl_2(Hpz^{R(n,n)iq}$)]				*Compounds [$PdBr_2(Hpz^{R(n,n)iq}$)]*			
4	**19**	Cr→Col_L→I	232 (8.4), 318[c,d]	12	**27**	Cr→Col_L→I	64 (6.4), 198 (18.9)
						I→Col_L→Cr	186 (-18.7), 50[c]
6	**20**	Cr→Cr'→Col_L→I	106 (1.8), 169 (0.2), 315[c,d]	14	**28**	Cr→Col_L→I	68 (20.7), 194 (21.0)
						I→Col_L→Cr	173 (-17.7), 62 (-4.1)
8	**21**	Cr→Cr'→Col_L→I	49 (1.1), 147 (2.4), 305[c,d]	16	**29**	Cr→Col_L→I	52 (18.2), 183 (12.5)
						I→Col_L→Cr	181 (-12.2), 51[c]
10	**22**	Cr→Col_L→I	63 (0.9), 279[e]	18	**30**	Cr→Cr'→Col_L→I	66 (60.9)[f], 187 (17.7)
						I→Col_L→Cr	181 (-18.0), 65 (-3.8)
12	**23**	Cr→Col_L→I	45 (1.2), 272[e]	*Compounds [$PdI_2(Hpz^{R(n,n)iq}$)]*			
14	**24**	Cr→Cr'→Col_L→I	49, 63 (18.6)[f], 268[e]	12	**31**	Cr→Col_L→I	56 (17.0), 160 (12.9)
						I→Col_L→Cr	156 (-13.7), 43[c]
16	**25**	Cr→Cr'→Col_L→I	80 (16.8)[f], 246[e]	14	**32**	Cr→Col_L→I	64 (11.8), 156 (11.6)
						I→Col_L→Cr	154 (-11.0), 62[c]
18	**26**	Cr→Cr'→Col_L→I	63, 83 (52.9)[f], 237[e]	16	**33**	Cr→Col_L→I	60 (32.8), 153 (13.0)
						I→Col_L→Cr	153 (-10.9), 65[c]
				18	**34**	Cr→Col_L→I	71 (92.2), 156 (12.9)
						I→Col_L→Cr	149 (-12.2), 48[c]

[a] Cr, Cr' = crystalline phases, Col_L = lamellar columnar mesophase, I = isotropic liquid. [b] DSC onset peaks. [c] Detected by POM. [d] Pronounced decomposition. [e] Enthalpy was not determined due to pronounced decomposition. [f] Overlapped processes.

the new dichloride Pd(II) compounds [$PdCl_2(Hpz^{R(n,n)iq})$] **19**-**26** (type **II**) also exhibit mesomorphism, regardless of the alkyl chain length. However, the observation by POM is not easy because of the pronounced decomposition that these derivatives undergo as a result of the high clearing temperatures reached. In order to minimise the thermal decomposition of the sample, the hot-plate of the microscope was previously heated at temperatures slightly above the clearing point. Then, the sample was placed and the temperature was decreased quickly. Although this method did not prevent the decomposition of the sample, some domains with birefringent spherulitic textures could be observed when the mesophase emerged from the isotropic liquid upon cooling (Figure 6a). Likewise, the new analogous dibromide and diiodide pyridylpyrazole Pd(II) compounds [$PdBr_2(Hpz^{R(n,n)py})$] **10**-**13** and [$PdI_2(Hpz^{R(n,n)py})$] **15**-**18** (type **I**) also show mesomorphic behaviour (Figure 6b,c) with the exception of the derivatives **9** and **14** bearing the shortest hexyloxy chains, which melt into the isotropic liquid directly from the solid at 230 and 195 ºC, respectively. This indicates that long alkyl chains are now required to induce mesomorphism in the dibromide and diiodide species, most likely to compensate the

View Article Online
DOI: 10.1039/C9TC03627J

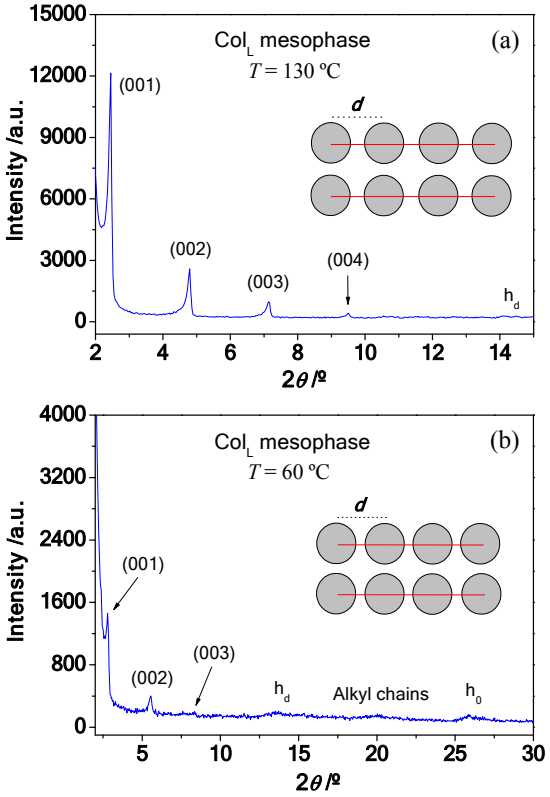

Figure 7 XRD diffractograms for (a) [$PdBr_2(Hpz^{R(18,18)py})$] **13** and (b) [$PdI_2(Hpz^{R(16,16)iq})$] **33**, registered at 130 and 60 ºC respectively.

increasing size of the halide ligands (in comparison with the chloride ones). Likewise, as it was expected, the related dibromide and diiodide isoquinolinylpyrazole compounds [$PdBr_2(Hpz^{R(n,n)iq})$] **27**-**30** and [$PdI_2(Hpz^{R(n,n)iq})$] **31**-**34** (type **II**) show mesomorphism, exhibiting the typical fan-like textures of a columnar mesophase (Figure 6d,e).

Tables 2 and 3 depict the phase transition temperatures and their associated enthalpy data measured by differential scanning calorimetry (DSC). In particular, the dichloride isoquinolinylpyrazole Pd(II) derivatives **19**-**26** show a pronounced decomposition that is clearly detected by POM due to the high clearing temperatures reached and therefore, the thermal data are not given on cooling.

The DSC thermograms of most of the compounds display a similar pattern upon heating, which is consistent with two endothermic peaks that can be attributed to the solid-mesophase (Cr-Col$_L$) and mesophase-isotropic liquid (Col$_L$-I) phase transitions in agreement with the POM observations (Figure S1). In some cases, a third peak associated with a phase transition in the solid state (Cr-Cr') is also registered before the melting temperature. On cooling, the corresponding exothermic peak attributed to the isotropic liquid-mesophase (I-Col$_L$) transition is clearly observed, but the solidification process is only detected in certain cases. This seems to indicate that a high degree of order in the supramolecular arrangement of the mesophase exists. Note that the enthalpy values of the mesophase-isotropic liquid phase transitions are

Table 4 XRD data for the prototype compounds **13**, **16**, **24**, **30** and **33**

	d-spacing (Å)	[*hkl*][a]	Parameters[e]
13	36.2, 18.5, 12.4, 9.3, 6.3, 4.7, 3.4	001, 002, 003, 004, h_d[b], alkyl[c], h_0[d]	*d* = 36.9 Å, T = 130 ºC.
16	29.4, 14.8, 9.8, 7.4, 6.5, 4.8, 3.4	001, 002, 003, 004, h_d[b], alkyl[c], h_0[d]	*d* = 29.5 Å, T = 110 ºC.
24	27.0, 13.6, 9.1, 6.8, 5.8, 4.7	001, 002, 003, 004, h_d[b], alkyl[c]	*d* = 27.2 Å, T = 140 ºC.
30	31.2, 15.8, 10.6, 7.9, 5.7, 4.8, 3.4	001, 002, 003, 004, h_d[b], alkyl[c], h_0[d]	*d* = 31.6 Å, T = 160 ºC.
33	31.4, 15.9, 11.1, 6.5, 4.5, 3.4	001, 002, 003, h_d[b], alkyl[c], h_0[d]	*d* = 32.2 Å, T = 60 ºC.

[a] [*hkl*] are the Miller indices of the reflections.[b] Broad halo attributed to the inter-dimer distance. [c] Broad halo associated with the liquid-like order of the molten alkyl chains. [d] Intracolumnar distance. [e] Lamellar periodicity: $d = (\Sigma l d_{00l})/N_{00l}$, where N_{00l} is the number of *00l* reflections.

rather high for all compounds, which is consistent with this hypothesis. In addition, severe restrictions that hinder the ordering of molecules during the formation of the mesophase upon cooling generate a large hysteresis with respect to the isotropisation process. As observed in Figure S1 for **10**, the isotropic liquid-mesophase transition occurs at 142 ºC whereas the corresponding mesophase-isotropic liquid transition occurs at 167 ºC. This constitutes further evidence that the mesophase may be highly-ordered.

It is interesting to mention that the mesomorphism depends on two key factors, the alkyl chain length and the nature of the ligands. For the sake of clarity, the melting and clearing temperatures of each series of compounds have been represented in the bar diagrams shown in Figures S2 and S3. The thermal data of the dichloride pyridylpyrazole Pd(II) compounds **1**-**8** previously described by us have been also included for comparative purposes.[15] The first aspect that attracts attention is that the mesophases of the dichloride derivatives show the widest stability ranges for both types of compounds, in comparison with the analogous dibromide and diiodide ones. Moreover, the effect of the chain length is also greater in these species. Unlike the dibromide and diiodide compounds (whose transition temperatures are practically maintained with increasing the chain length), the melting point of the dichloride derivatives notably varies as a function of the strength of both the van der Waals interactions between the hydrophobic chains (prevailing when n > 10) and the intermolecular interactions between the disc-like units (prevailing when n ≤ 10). Thus, the compound **23** with 12 carbon atoms at the alkyl chains shows the lowest melting temperature because the strength of the Van der Waals interactions between the alkyl chains are still relatively weak in the solid state, which favour the establishment of new interactions between the disc-like units that are required for achieving the supramolecular organisation in the mesophase. Likewise, the clearing temperatures generally decrease by increasing the chain length. The high mobility induced by long chains leads to weaker intermolecular interactions in the mesophase and, therefore, it transforms into the isotropic liquid at lower temperatures.

View Article Online
DOI: 10.1039/C9TC03627J

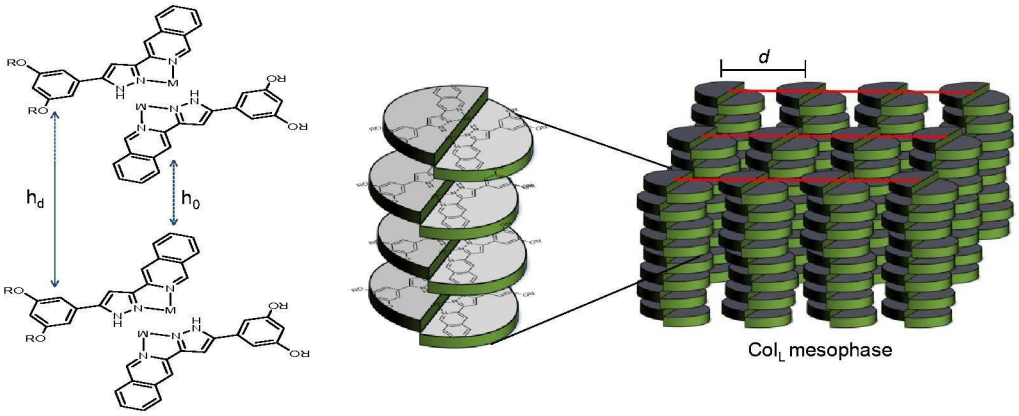

Figure 8 Schematic model showing the self-assembly of molecules in the Col_L mesophase. The interdimer (h_d) and intracolumnar (h_o) distances are indicated.

The polarisation and the size of the halide ligands also show a direct influence on the thermal behaviour. The melting temperatures of the dichloride derivatives are lower than those found for the analogous dibromide and diiodide compounds for the compounds of type I, but this effect is less pronounced for the species containing the isoquinolinyl group that melt at similar temperatures of *ca*. 50 – 80 ºC. However, the clearing points decrease by increasing the size of the halide ligands for both families, as expected.

However, not only the halide ligands display a remarkable change in the mesomorphic properties, but the increase of the π-conjugation induced by the presence of the isoquinoline group (in comparison with the pyridine moiety) causes a decrease of the melting temperatures and an increase of the clearing ones. In fact, this effect prevails over the influence of the halide ligands, which explains why the dichloride isoquinolinylpyrazole Pd(II) derivatives show similar melting temperatures than those found in related dibromide and diiodide compounds. Therefore, on the basis of all the above-mentioned considerations, the dichloride isoquinolinylpyrazole Pd(II) compounds $[PdCl_2(Hpz^{R(n,n)iq})]$ exhibit the best liquid crystal behaviour.

Variable-temperature XRD experiments allowed establishing the lamellar columnar nature of the mesophase, and the highly-ordered columnar arrangement of molecules could be confirmed. As a representative example, Figure 7a shows a detail of the low-angle X-ray pattern for the compound $[PdBr_2(Hpz^{R(18,18)py})]$ **13**, recorded in the liquid crystal state at 130 ºC. The diffractogram clearly displays four peaks that can be well-indexed as the (001), (002), (003) and (004) reflections of a lamellar lattice. Similar results were obtained for all the compounds analysed (see Table 4), although the fourth order reflection of the layer was not always observed.

As shown in Figure 7b for the diiodide derivative $[PdI_2(Hpz^{R(16,16)iq})]$ **33**, several peaks also appear in the medium-angle region between 10 and 30º. Firstly, a broad diffraction peak is clearly displayed at around 3.4 Å, which is also observed in most of the studied compounds. This reflection is associated with the intracolumnar distance h_0 in highly-ordered discotic liquid crystals. Note that this peak was not detected for the dichloride isoquinolinylpyrazole compound **24** nor for the analogous pyridylpyrazole derivatives **1** and **6** previously described. This indicates that the columnar arrangement in these two families presents a certain degree of disorder. Secondly, a low-intense peak is observed at *ca*. 6.5 Å, which is shown for all compounds. This peak may be related with the fact that molecules can establish intermolecular interactions in the mesophase, so that the discotic shape required for inducing the lamellar columnar mesophase may be generated through the formation of head-to-tail dimers, as demonstrated above in the crystal structure of $[PdBr_2(Hpz^{R(6,6)py})]$ **9**. Under such considerations, the diffraction peak that appears at 6.5 Å can be attributed to the interdimer distance h_d in the mesophase (see Figure 8). Last, the typical diffuse and broad peaks of the molten alkyl chains are observed at *ca*. 4.5 – 4.7 Å in all cases.

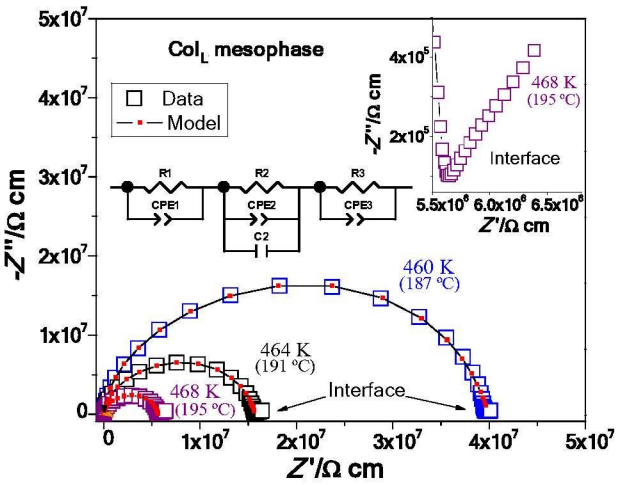

Figure 9 *-Z''* vs. *Z'* plots for the dibromide Pd(II) compound $[PdBr_2(Hpz^{R(12,12)iq})]$ **27** in the Col_L mesophase upon increasing the temperature. The inset shows a magnification of the pike-like contribution at high frequencies.

View Article Online
DOI: 10.1039/C9TC03627J

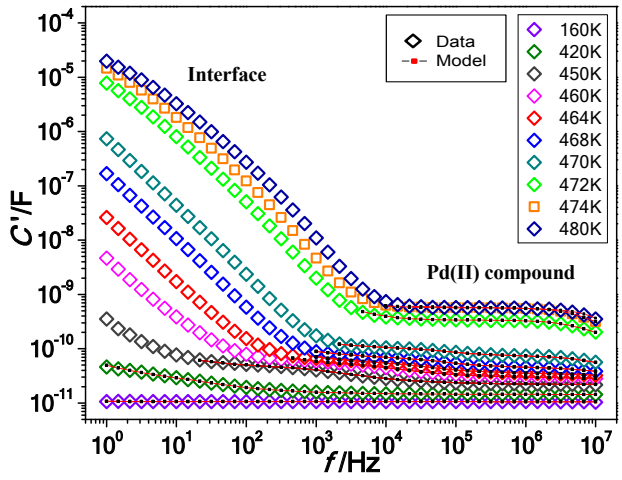

Figure 10 C' vs. f plots for the dibromide Pd(II) compound [$PdBr_2(Hpz^{R(12,12)iq})$] **27** in the solid, mesophase and isotropic liquid phases at selected temperatures.

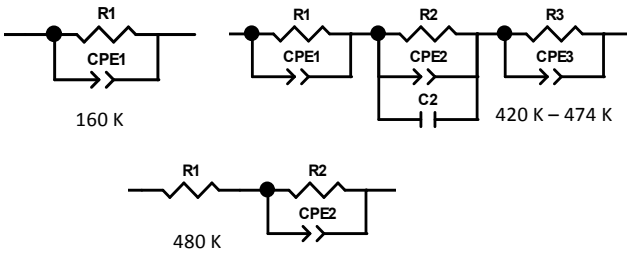

Figure 11 Equivalent circuits used to fit the impedance data.

Dielectric spectroscopy and conductivity measurements

All the Pd(II) metallomesogens reported herein are susceptible to exhibit proton conduction as a result of the dissociation of the acidic pyrazole proton (named H2; see Figures 1 and 3). Note that molecules are self-assembled in a lamellar columnar organisation and therefore, these metallomesogens may act as 2D conductors in the temperature range of the Col_L mesophase.[12] Also, the high fluidity of the liquid crystal state may favour the proton transport under anhydrous conditions, which is why these materials are of great interest for the development of proton exchange membrane (PEM) fuel cells with moderate and high operational temperatures.[10] In this context, the dielectric behaviour of the prototype compounds **2**, **5**, **8**, **10**, **15**, **23**, **27** and **31** have been studied by temperature-dependent impedance spectroscopy in the Col_L mesophase, in the solid state, and in the isotropic liquid phase.

Complex impedance plots of imaginary (-Z'') vs. real (Z') part of the impedance show an infinite resistance to the charge transport from 160 K until temperatures near to the melting point of the compounds. This indicates that the Pd(II) compounds behave as insulating materials in the solid state. By contrast, several dielectric contributions are observed at the mesophase temperatures (Fig. 9). On the one hand, the semicircle related to the charge transport within the material appears in the high-medium frequency region. Note that its

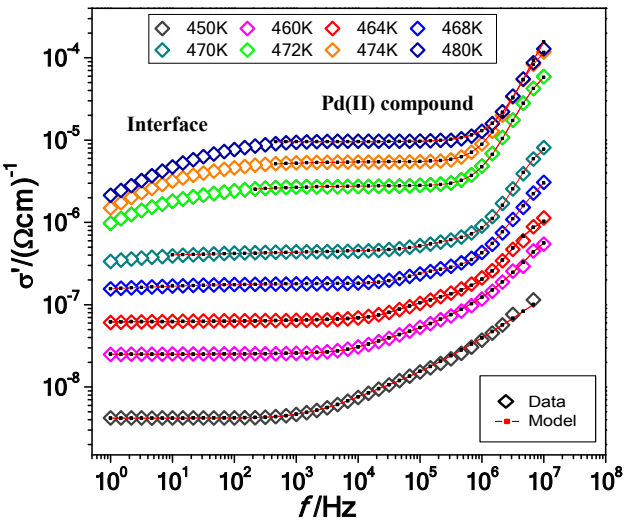

Figure 12 σ' vs. f plots for the dibromide Pd(II) compound [$PdBr_2(Hpz^{R(12,12)iq})$] **27** in the solid, mesophase and isotropic liquid phases at selected temperatures.

diameter decreases with increasing the temperature, that is the resistivity of the material decreases, which is consistent with a conduction mechanism mainly of ionic nature. The semicircles also show a non-symmetrical shape, which can be interpreted as the overlap of several semicircles. This in turn suggests the presence of several dielectric contributions in the sample, which implies a heterogeneous charge transport. The impedance data could be well-modelled by using two or three R-CPE elements consisting in a resistor (R) and a constant phase element (CPE) that represents the non-ideality of the dielectric contribution.

The use of an additional ideal capacitor in series in one of the R-CPE elements was required in some cases to achieve a good fit of the impedance data at high frequencies, i.e. leading to an R-CPE-C element. The typical pike-like dielectric contribution associated with the blocking of the ion transport at the sample/electrode interface is also recorded at low frequencies.[17]

As shown in Figure S4 for **27**, the ionic charge transport is maintained in the isotropic liquid phase, as indicated again by the typical pike-like feature at low frequencies. The resistivity of the Pd(II) metallomesogens is rather low at these temperatures, so that the blocking of the charge carriers at the interface between the sample and the metallic electrodes can be observed more clearly in form of a larger pike-structure.

The resistance of ionic conductivity is considerably lower as compared to the columnar mesophase, because the ions may move more freely in the isotropic liquid. The impedance data were fitted by using a single resistor and a R-CPE element in series in the isotropic liquid phase. The single resistor is associated with a small non-zero intercept of the data with the real Z' x-axis near 20 Ohm, which can be interpreted as a residual resistance of the measurement cables, electrodes and the liquid cell.

Similar features were found for all the Pd(II) compounds regardless the nature of the ligands and the alkyl chain length.

View Article Online
DOI: 10.1039/C9TC03627J

The impedance data were converted into capacitance and conductivity notations in order to analyse the dielectric behaviour of these compounds as a function of temperature in their different phases. Figure 10 shows the *C'* vs. *f* curves for the prototype Pd(II) compound **27** at selected temperatures. As observed, the capacitance remains uniform for all measured frequencies in the solid state, showing values of the order of 1.0 x 10^{-11} F. Upon heating the sample, the heterogeneous conduction in the Col_L mesophase is evidenced by the formation of two C' plateaus in the middle- and low-frequency region. It is noteworthy that an additional C' plateau is observed at temperatures above 420 K. This feature is most likely related to the formation of new conduction pathways due to an increment in the degree of freedom of movement of the molecules, which may favour the mobility of the ionic charge carriers. Note that a single plateau is again formed in the isotropic liquid state, where the lamellar columnar organisation of molecules is lost and therefore, the charges carriers can move freely. It is also interesting to observe that the capacitance gradually increases with temperature until the sample reaches 470 K. No significant changes are observed during the solid-mesophase transition, probably because the supramolecular organisation is similar in both phases. However, a remarkable jump is detected in the temperature range of 470 - 472 K in accordance with the formation of the isotropic liquid. Likewise, the charge blocking at the sample/electrode interface is manifested by an abrupt increase of the capacitance values at low frequencies. The effect is more pronounced as the temperature increases, as expected for an ionic conductor. The equivalent circuits used to fit the impedance data at different temperatures are shown in Figure 11.

The temperature dependence of the σ' vs. *f* curves supports all the considerations discussed above. Several thermally-activated plateaus appear at low and intermediate frequencies, confirming once again that the charge transport inside the material occurs through different pathways that open up in the Col_L mesophase (Figure 12). The diffusion of charge carriers into the metal electrodes is also observed in form of a decrease of the intrinsic conductivity of **27** at low frequencies (Interface). Likewise, the Jonscher's universal dielectric response law could be verified at high frequencies for all temperatures measured.[18] This feature allowed obtaining the Jonscher exponent, whose value was found to be *n* = 0.92.

To further analyse the dielectric behaviour from the solid to the isotropic liquid, *C'* vs. *T* and σ' vs. *T* were plotted together as shown in Figure 13 for **27**. Regarding the capacitance measurements two abrupt changes at 67 and 200 ºC are observed, which can be attributed to the solid-mesophase and mesophase-isotropic liquid phase transitions. The charge transport also begins at 67 ºC when continuous pathways are opened in the Col_L mesophase. In accordance with a proton conductor, the conductivity of **27** increases proportionally with temperature during the overall existence range of the mesophase, and only at the clearing temperature a remarkable change in the intercept is detected. A similar

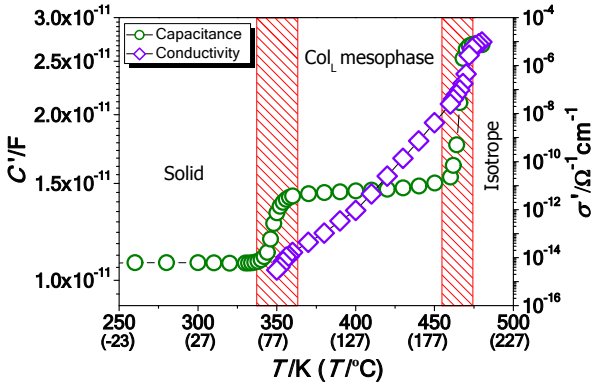

Figure 13 *C'* and σ' vs. *T* plots for [$PdBr_2$($Hpz^{R(12,12)iq}$)] **27** upon increasing the temperature from the solid to the isotropic liquid. The capacitance was measured at 10 MHz and the conductivity values were extracted from equivalent circuit fits. The red shaded areas show the solid-mesophase and mesophase – isotropic liquid phase transitions.

Table 5 Maximum conductivity values measured in the mesophase and in the isotropic phase.

Comp.	$\sigma'_{mesophase}$ / (Ω cm)$^{-1}$	$\sigma'_{isotropic\ liquid}$ / (Ω cm)$^{-1}$	$Ea_{mesophase}$ / eV
2	3.19×10^{-5}	-	2.71
5	3.04×10^{-7}	1.56×10^{-6}	2.76
8	1.42×10^{-7}	1.36×10^{-6}	2.09
10	2.91×10^{-9}	1.76×10^{-6}	1.76
15	1.88×10^{-6}	3.98×10^{-6}	1.97
23	2.75×10^{-5}	-	1.46
27	4.43×10^{-7}	9.61×10^{-6}	1.76
31	5.57×10^{-8}	1.51×10^{-6}	2.48

behaviour is observed for all the metallomesogens analysed, although the maximum conductivity value reached in the Col_L mesophase is different for each compound. The highest conductivities are found for the dichloride Pd(II) derivatives **2** and **23** with values of 3.19 x 10^{-5} and 2.75 x 10^{-5} Ω^{-1} cm^{-1}, respectively (Table 5). This fact can be understood by considering that these compounds have clearing points higher than those found in the related dibromide and diiodide species. Therefore, since the mesophase reaches higher temperatures, higher conductivities in the mesophase can be obtained. In the isotropic phase where the conduction pathways are broken and protons can move freely, all the compounds show similar conductivity values of the order of 10^{-6} Ω^{-1} cm^{-1}.

The activation energies have been determined from the Arrhenius equation by plotting Ln(σ') vs. 1/*T* (not shown) in the temperature range of the Col_L mesophases. The values are ranging between 1.46 and 2.76 eV (Table 5), where the pyridylpyrazole dichloride Pd(II) compounds are the metallomesogens with the highest activation energies for proton conduction.

Upon cooling the samples to room temperature, the conductivity progressively decreases until the formation of the solid phase, where these metallomesogens behave as

View Article Online
DOI: 10.1039/C9TC03627J

insulating materials. In general terms, the dielectric behaviour of the compounds shows a good reversibility with the exception of the dichloride compounds **2** and **23**, which show a pronounced decomposition at temperatures close to the clearing point.

Experimental section

Materials and methods

All commercial chemicals and solvents were purchased from Sigma-Aldrich or Alfa-Aesar and used without further purification. The 3-(3,5-bis(alkyloxy)phenyl)-(5-pyridin-2-yl)pyrazole and 3-(3,5-bis(alkyloxy)phenyl)-(5-isoquinolin-2-yl)pyrazole ligands [$Hpz^{R(n,n)py}$] and [$Hpz^{R(n,n)iq}$] have been obtained by a condensation reaction between the corresponding diketone and hydrazine monohydrate in refluxing ethanol, as it was described in several previous works by us.[15, 19]

The elemental analyses of C, H and N were performed by the Microanalytical Service of the Complutense University of Madrid (validated range: %C 0.5–94.7, %H 0.5–7.6, %N 0.5–23.0). The infra-red spectra were recorded on a FTIR Thermo Nicolet 200 spectrophotometer with samples as KBr pellets in the 4000–400 cm^{-1} region: w (weak), m (medium) and s (strong). ^1H and ^{13}C NMR, 2D COSY, selective 1D NOESY, ^1H-^{13}C HMQC, and ^1H-^{13}C HMBC spectra were carried out on a Bruker DPX-300 spectrophotometer from the NMR Service of the Complutense University of Madrid. All measurements were made with the samples in $CDCl_3$ solutions at room temperature. Chemical shifts δ are listed relative to $SiMe_4$ by using the signal of the deuterated solvent as a reference (7.26 and 77.0 ppm for ^1H and ^{13}C, respectively) and coupling constants *J* are given in hertz. Multiplicities are indicated as follows: s (singlet), d (doublet), t (triplet), pt (pseudo-triplet), qt (quintet), ddd (doublet of doublets of doublets), m (multiplet). The ^1H and ^{13}C chemical shifts are accurate to ±0.01 and ±0.1 ppm, respectively, and coupling constants to ±0.3 Hz.

Polarised optical microscopy observations were carried out by using an Olympus BX50 microscope equipped with a Linkam THMS 600 heating stage. The transition temperatures and their associated enthalpy data were determined with a Perkin Elmer Pyris 1 differential scanning calorimeter. Samples were sealed hermetically in aluminium pans and measurements were made with heating and cooling rates of 10 K min^{-1}. Temperature-dependent powder X-ray diffraction studies were carried out on a Panalytical X'Pert PRO MPD diffractometer with Cu-Kα (1.54 Å) radiation in a ϑ–ϑ configuration equipped with an Anton Paar HTK1200 heating stage (X-Ray Diffraction Service of the Complutense University of Madrid).

The dielectric properties of the complexes in the solid, liquid crystal and isotropic liquid phases were measured by alternating current (AC) impedance spectroscopy using an Alpha Analyser integrated into the Novocontrol BDS 80. Measurements were performed at a frequency (*f*) range of 1 Hz – 10 MHz with 6 measurements points per frequency decade, using a 0.1 V applied AC voltage signal. The temperature (*T*) was varied between 160 K and the clearing point of the compounds or the upper instrumental limit of 562 K (-113 ºC – 289 ºC) upon heating and cooling cycles. Dielectric data were taken under steady state conditions, i.e. the temperature was stabilised for 3 – 10 minutes before taking impedance measurements over the full *f*-range. The temperature increments/reductions for taking impedance measurements were 20 K – 2 K steps. In particular, the temperature was increased/decreased in smaller steps near the phase transitions. The complexes in the solid state were placed between the polished electrodes of a custom-built stainless-steel liquid cell with a high surface to thickness ratio. The cell was closed with a sapphire plate and placed inside the Novocontrol cryostat.

The dielectric response of the materials was obtained at selected temperatures for heating and cooling cycles in terms of the real and imaginary parts (Z', Z'') of the complex impedance $Z^* = Z' + iZ''$. The data were converted into the complex conductivity σ^* and capacitance C^* notations, $\sigma^* = \sigma' + i\sigma''$ and $C^* = C' - iC''$, using the standard conversions: $Z^* = (g\sigma^*)^{-1}$, and $Z^* = (i\omega C^*)^{-1}$, where *g* (in cm) is the geometrical factor given by electrode area divided by electrode distance, ω is the angular frequency. The geometrical factor *g* could only be estimated from the weight and density of the powder measured initially, and the measurement cell dimensions. Equivalent circuit fitting of the dielectric data was performed by using Z-View software.

Synthesis of complexes [$PdCl_2(Hpz^{R(n,n)py})$] 1-8

The dichloride Pd(II) compounds [$PdCl_2(Hpz^{R(n,n)py})$] **1**-**8** were obtained by reaction between the corresponding pyrazole [$Hpz^{R(n,n)py}$] and bis(benzonitrile)dichloridepalladium(II) in dichloromethane solution at reflux temperature. The procedure followed and the full characterisation of the compounds were previously reported by us.[15]

Synthesis of complexes [$PdBr_2(Hpz^{R(n,n)py})$] 9-13

A solution of the corresponding pyrazole [$Hpz^{R(n,n)py}$] (0.38 mmol) and Pd(II) bromide (0.38 mmol, 101 mg) in a mixture of dichloromethane (20 mL) and acetonitrile (5 mL) was refluxed for 24 h. Next, the reaction mixture was concentrated under vacuum and filtered over Celite®. The precipitate obtained after adding acetonitrile (*ca.10* mL) was filtered off and dried *in vacuum* to give the corresponding Pd(II) complex as an orange solid.

All compounds were characterised by IR, ^1H-NMR and CHN elemental analyses (deposited as ESI†). Additionally, the prototype complex [$PdBr_2(Hpz^{R(12,12)py})$] **10** was also characterised by ^{13}C-NMR. Their spectroscopic data and elemental analyses are shown below as a representative example of this family.

[$PdBr_2(Hpz^{R(12,12)py})$] (10): orange solid (58%). Found: C, 54.0; H, 6.8; N, 5.1. $PdC_{38}H_{59}N_3O_2Br_2 \cdot 0.3CH_3CN$ requires C, 53.4; H, 7.0; N, 5.3%. ν_{max}/cm^{-1}: 3260m ν(N–H), 2921 – 2851s $\nu(C–H)_{aliph}$, 1597s ν(C=C + C=N), 779m $\gamma(C–H)_{py}$. δ_H (300.16

View Article Online
DOI: 10.1039/C9TC03627J

MHz; $CDCl_3$; TMS): 0.88 (6H, t, ^3J 6.9, CH_3), 1.27 (36H, m, CH_2), 1.80 (4H, qt, ^3J 6.7, CH_2), 2.10 (s, CH_3CN), 3.98 (4H, t, ^3J 6.5, OCH_2), 6.53 (1H, t, ^4J 2.0, Hp), 6.63 (2H, d, ^4J 2.1, Ho), 7.04 (1H, s, H4'), 7.41 (1H, ddd, ^3J 7.3, 5.7, ^4J 1.3, H5), 7.90 (1H, d, ^3J 7.4, H3), 8.08 (1H, ddd, ^3J 7.7, 7.7, ^4J 1.4, H4), 9.25 (1H, d, ^3J 5.7, H6), 11.00 (1H, s, NH). δ_C (75.48 MHz; $CDCl_3$; TMS): 14.1 (CH_3), 22.7 – 31.9 (CH_2), 68.5 (OCH_2), 102.4 (C4'), 103.4 (Cp), 104.0 (Co), 123.1 (C3), 125.2 (C5), 127.2 (Ci), 140.6 (C4), 145.5 (C3'), 150.1 (C2), 151.7 (C6), 152.1 (C5'), 161.0 (Cm).

Synthesis of complexes [$PdI_2(Hpz^{R(n,n)py}$)] 14-18

The compounds were obtained by reaction of the corresponding pyrazole [$Hpz^{R(n,n)py}$] (0.28 mmol) with Pd(II) iodide (0.28 mmol, 101 mg), using the same procedure to that above described for [$PdBr_2(Hpz^{R(n,n)py})$].

The spectroscopic data and the elemental analyses of [$PdI_2(Hpz^{R(12,12)py})$] **15** are shown below as a representative example of all iodide palladium compounds (deposited as ESI†).

[$PdI_2(Hpz^{R(12,12)py})$] (15): red solid (67%). Found: C, 48.0; H, 6.1; N, 4.5. $PdC_{38}H_{59}N_3O_2I_2$ requires C, 48.0; H, 6.3; N, 4.4%. ν_{max}/cm^{-1}: 3308m ν(N–H), 2920 – 2850s $\nu(C–H)_{aliph}$, 1595m ν(C=C + C=N), 778m $\gamma(C–H)_{py}$. δ_H (300.16 MHz; $CDCl_3$; TMS): 0.88 (6H, t, ^3J 6.9, CH_3), 1.27 (36H, m, CH_2), 1.81 (4H, qt, ^3J 6.6, CH_2), 3.99 (4H, t, ^3J 6.5, OCH_2), 6.53 (1H, t, ^4J 2.0, Hp), 6.64 (2H, d, ^4J 1.9, Ho), 6.98 (1H, d, ^4J 1.9, H4'), 7.41 (1H, ddd, ^3J 7.5, 5.8, ^4J 1.2, H5), 7.87 (1H, d, ^3J 7.5, H3), 8.08 (1H, ddd, ^3J 7.7, 7.7, ^4J 1.4, H4), 9.51 (1H, d, ^3J 5.8, H6), 11.03 (1H, d, ^4J 1.4, NH). δ_C (75.48 MHz; $CDCl_3$; TMS): 14.1 (CH_3), 22.7 – 31.9 (CH_2), 68.5 (OCH_2), 102.6 (C4'), 103.1 (Cp), 104.0 (Co), 123.2 (C3), 125.5 (C5), 127.2 (Ci), 140.3 (C4), 145.2 (C3'), 150.1 (C2), 152.5 (C5'), 153.1 (C6), 161.0 (Cm).

Synthesis of complexes [$PdCl_2(Hpz^{R(n,n)iq}$)] 19-26

Dichloride isoquinolinylpyrazole Pd(II) compounds were obtained from the reaction between the corresponding isoquinolinylpyrazole compound [$Hpz^{R(n,n)iq}$] (0.26 mmol) and bis(benzonitrile)dichloridepalladium(II) (0.26 mmol, 99.72 mg) in 20 mL of dichloromethane. The reaction mixture was refluxed during 24 h. After concentrating the solution under vacuum, it was filtered over Celite®. Addition of acetonitrile (*ca.* 10 mL) gave a pale orange precipitate, which was filtered off and dried in vacuum.

All compounds were characterised by IR, ^{1}H-NMR and CHN elemental analyses (deposited as ESI†). Additionally, the prototype complex [$PdCl_2(Hpz^{R(12,12)iq})$] **23** was also characterised by ^{13}C-NMR. Their spectroscopic data and elemental analyses are shown below as a representative example of this family.

[$PdCl_2(Hpz^{R(12,12)iq})$] (23): pale orange solid (67%). Found: C, 62.1; H, 7.3; N, 5.1. $PdC_{42}H_{61}N_3O_2Cl_2$ requires C, 61.7; H, 7.5; N, 5.1%. ν_{max}/cm^{-1}: 3272w ν(N–H), 2921 – 2852s $\nu(C–H)_{aliph}$, 1637 – 1595s ν(C=C + C=N), 754 – 717m $\gamma(C–H)_{iq}$. δ_H (300.16 MHz; $CDCl_3$; TMS): 0.88 (6H, t, ^3J 6.9, CH_3), 1.27 (36H, m, CH_2), 1.81 (4H, qt, ^3J 6.8, CH_2), 3.98 (4H, t, ^3J 6.3, OCH_2), 6.50 (1H, t, ^4J 1.9, Hp), 6.56 (2H, d, ^4J 2.0, Ho), 7.29 (1H, d, ^4J 1.6, H4'), 7.65 (2H, m, H7, H8), 7.94 (1H, pt, ^3J 7.1, H6), 8.09 (1H, d, ^3J 7.9, H5), 8.40 (1H, s, H4), 9.19 (1H, s, H1), 10.58 (1H, br, NH). δ_C (75.48 MHz; $CDCl_3$; TMS): 14.1 (CH_3), 22.6 – 31.9 (CH_2), 68.5 (OCH_2), 101.4 (C4'), 103.2 (Co), 103.9 (Cp), 120.8 (C4), 126.6 (Ci), 126.9 (C10), 128.0 (C5), 128.7 (C8), 129.7 (C7), 134.0 (C6), 135.2 (C9), 141.9 (C3), 145.0 (C3'), 151.7 (C5'), 154.1 (C1), 160.9 (Cm).

Synthesis of complexes [$PdBr_2(Hpz^{R(n,n)iq}$)] 27-30

Dibromide isoquinolinylpyrazole Pd(II) compounds were obtained by a reaction of the corresponding isoquinolinylpyrazole compound [$Hpz^{R(n,n)iq}$] and palladium(II) bromide in a 1 : 1 (ligand : metal) molar ratio, according to the procedure above-described for the related dibromide pyridylpyrazole Pd(II) compounds [$PdBr_2(Hpz^{R(n,n)py})$]. All compounds were isolated as orange solids. The spectroscopic data and elemental analyses are given in ESI†. In particular, [$PdBr_2(Hpz^{R(12,12)py})$] **27** was also characterised by ^{13}C-NMR spectroscopy as a representative example.

[$PdBr_2(Hpz^{R(12,12)iq})$] (27): orange solid (62%). Found: C, 55.7; H, 6.6; N, 4.7. $PdC_{42}H_{61}N_3O_2Br_2$ requires C, 55.7; H, 6.8; N, 4.6%. ν_{max}/cm^{-1}: 3325w ν(N–H), 2917 – 2850s $\nu(C–H)_{aliph}$, 1635 – 1595m ν(C=C + C=N), 754 – 717m $\gamma(C–H)_{iq}$. δ_H (300.16 MHz; $CDCl_3$; TMS): 0.88 (6H, t, ^3J 7.0, CH_3), 1.27 (36H, m, CH_2), 1.82 (4H, qt, ^3J 6.6, CH_2), 3.99 (4H, t, ^3J 6.5, OCH_2), 6.52 (1H, t, ^4J 2.0, Hp), 6.57 (2H, d, ^4J 2.0, Ho), 7.23 (1H, d, ^4J 1.9, H4'), 7.65 (2H, m, H7, H8), 7.94 (1H, ddd, ^3J 8.1, 5.7, ^4J 1.4, H6), 8.09 (1H, d, ^3J 8.2, H5), 8.38 (1H, s, H4), 9.46 (1H, s, H1), 10.64 (1H, d, ^4J 1.6, NH). δ_C (75.48 MHz; $CDCl_3$; TMS): 14.1 (CH_3), 22.7 – 31.9 (CH_2), 68.5 (OCH_2), 101.4 (C4'), 103.3 (Co), 103.7 (Cp), 120.8 (C4), 126.9 (Ci), 127.0 (C10), 128.0 (C5), 128.7 (C8), 129.6 (C7), 133.9 (C6), 135.1 (C9), 141.9 (C3), 144.8 (C3'), 151.9 (C5'), 155.2 (C1), 160.8 (Cm).

Synthesis of complexes [$PdI_2(Hpz^{R(n,n)iq}$)] 31-34

Diiodide isoquinolinylpyrazole Pd(II) compounds were obtained by a reaction of the corresponding isoquinolinylpyrazole compound [$Hpz^{R(n,n)iq}$] and palladium(II) iodide in a 1 : 1 (ligand : metal) molar ratio. The procedure was similar to that previously described for the related diiodide pyridylpyrazole Pd(II) compounds [$PdI_2(Hpz^{R(n,n)py})$].

The spectroscopic data and the elemental analyses of [$PdI_2(Hpz^{R(12,12)iq})$] **31** are given below as a representative example of all iodide palladium compounds (given in ESI†).

[$PdI_2(Hpz^{R(12,12)iq})$] (31): red solid (55%). Found: C, 50.7; H, 6.1; N, 4.3. $PdC_{42}H_{61}N_3O_2I_2$ requires C, 50.4; H, 6.2; N, 4.2%. ν_{max}/cm^{-1}: 3381w ν(N–H), 2924 – 2855m $\nu(C–H)_{aliph}$, 1597s ν(C=C + C=N), 770 – 725m $\gamma(C–H)_{iq}$. δ_H (300.16 MHz; $CDCl_3$; TMS): 0.88 (6H, t, ^3J 6.9, CH_3), 1.27 (36H, m, CH_2), 1.82 (4H, qt, ^3J 6.8, CH_2), 4.00 (4H, t, ^3J 6.5, OCH_2), 6.52 (1H, t, ^4J 1.9, Hp), 6.58 (2H, d, ^4J 2.0, Ho), 7.11 (1H, d, ^4J 1.8, H4'), 7.66 (1H, pt, ^3J 7.3, H7), 7.76 (1H, d, ^3J 8.0, H8), 7.93 (1H, ddd, ^3J 7.8, 6.7, ^4J 1.0, H6), 8.08 (1H, d, ^3J 8.1, H5), 8.28 (1H, s, H4), 9.81 (1H, s, H1), 10.73 (1H, br, NH). δ_C (75.48 MHz; $CDCl_3$; TMS): 14.1 (CH_3), 22.7 – 31.9 (CH_2), 68.5 (OCH_2), 101.6 (C4'), 103.3 (Cp), 103.6 (Co), 120.6 (C4), 127.0 (Ci), 127.7 (C10), 128.2 (C5), 128.7 (C8),

View Article Online
DOI: 10.1039/C9TC03627J

129.5 (C7), 133.7 (C6), 135.0 (C9), 142.2 (C3), 144.5 (C3'), 152.4 (C5'), 156.8 (C1), 160.9 (Cm).

X-Ray data collection and structure refinement

Data collection for single crystals of **9**·CH_3CN was carried out at room temperature on a Xcalibur, Atlas CCD diffractometer, operating at 50 kV and 40 mA with exposure times of 30 s, of 20 s, using graphite-monochromated Mo-Kα radiation (λ=0.71073 Å).

Data collection for **19** was carried out at room temperature on a Bruker Smart CCD diffractometer using graphite-monochromated Mo-Kα radiation (λ=0.71073 Å) operating at 50 kV and 35 mA. The data were collected over a hemisphere of the reciprocal space by combination of three exposure sets. Each exposure of 20 s covered 0.3 in ω. The cell parameters were determined and refined by a least-squares fit of all reflections. The first 100 frames were recollected at the end of the data collection to monitor crystal decay, and no appreciable decay was observed. A semi-empirical adsorption correction was applied.

A summary of the fundamental crystal and refinement data for both structures is given in Table 6.

The structures were solved by direct methods and refined by full-matrix least-squares procedures on F^2 (SHELXL-97).[20]

All non-hydrogen atoms were refined anisotropically. All hydrogen atoms were included in their calculated positions and refined riding on the respective bonded atoms, with some exceptions for **19**. Thus, the hydrogen H2 bonded to N2, was located in a Fourier synthesis and refined riding on the nitrogen atom. All carbon atoms of the chain have been refined using geometrical restrains and a variable common carbon-carbon distance.

CCDC 1937943 and 1937944 contain the supplementary crystallographic data for this paper. These data can be obtained free of charge from The Cambridge Crystallographic Data Centre via www.ccdc.cam.ac.uk/data_request/cif.

Table 6 Crystal data and structure refinement for **9**·CH_3CN and **19**

	9·CH_3CN	**19**
Empirical formula	$C_{28}H_{38}Br_2N_4O_2Pd$	$C_{26}H_{29}Cl_2N_3O_2Pd_1$
Formula weight /g mol^{-1}	728.84	592.82
Crystal system	Monoclinic	Orthorhombic
Space group	C2/c	*P*bca
a/Å	14.507(2)	16.818(9)
b/Å	21.421(2)	11.993(7)
c/Å	20.041(2)	25.531(2)
α/°	90	90
β/°	92.03(1)	90
γ/°	90	90
V/Å^3	6223.9(2)	5150.4(5)
Z	8	8
T/K	293(2)	293(2)
F(000)	2928	2416
ρ_c /g cm^{-3}	1.556	1.529
μ/mm^{-1}	3.194	0.956
Scan technique	ω and Φ	ω and Φ
Data collected	(-17, -25, -21) to (17, 25, 23)	(-20, -14, -30) to (15, 14, 25)
θ Range/º	3.32 to 25.00	1.60 to 25.00
Reflections collected	23837	37372
Independent reflections	5483 (R_{int}= 0.0529)	4543 (R_{int}= 0.0944)
Completeness to máximum θ (%)	99.8	100
Data/restraints/parameters	5483/0/334	4543/6/308
Observed reflections [$I > 2\sigma(I)$]	3667	2719
R^a	0.0451	0.0509
$R_{wF}{}^b$	0.1422	0.1808

^{a} $\Sigma(|F_o|-|F_c|)/\Sigma|F_o|$. ^{b} $[\Sigma(w(F_o^2-F_c^2)^2)/\Sigma(w(F_o^2)^2)]^{1/2}$

Conclusions

Several series of pyridyl- and isoquinolinylpyrazole dihalide Pd(II) compounds have been synthesised. The new compounds exhibit a half-disc molecular shape, but they are self-assembled into head-to-tail dimers, generating a disc-like shape that is adequate for achieving the supramolecular organisation required in the mesophase. Thermal studies reveal the existence of liquid crystal properties, which are maintained in high temperature ranges of up to 200 ºC. By modifying the nature of the ligands and the length of the terminal alkyl chains, the melting and clearing temperatures can be modulated. The introduction of the isoquinoline group at the pyrazole ligand in combination with alkyl chains of intermediate length and the presence of chloride ligands allowed obtaining materials that exhibit lamellar columnar mesophases near room temperature. Moreover, in the mesophases nanochannels are opened, which can be used for water-free proton conduction. The fluid properties in the liquid crystal were shown to favour the dissociation of the acidic pyrazole proton, and these metallomesogens therefore behave as proton conductors under anhydrous conditions. The use of metallomesogens as electrolytes may give access to the fabrication of a novel generation of PEM fuel cells that operate at moderate and high temperatures. To the best of our knowledge these materials constitute the first example of metallomesogens that exhibit proton conduction in lamellar columnar mesophases near to room temperature.

Conflicts of interest

There are no conflicts to declare.

Acknowledgements

The authors thank to the Spanish Ministerio de Economía y Competitividad (project CTQ2015-63858-P (MINECO/FEDER)) for funding. C. Cuerva acknowledges the Universidad Complutense de Madrid for his predoctoral contract (Programa de Financiación de Universidad Complutense de Madrid-Santander Universidades).

View Article Online
DOI: 10.1039/C9TC03627J

Notes and references

1 (a) T. A. H. Ratlamwala, A. H. El-Sinawi, M. A. Gadalla and A. Aidan, *Int. J. Energ. Res.*, 2012, **36**, 1121; (b) P. Y. Yi, L. F. Peng, X. M. Lai, Z. Q. Lin and J. Ni, *Fuel Cells*, 2012, **12**, 1019; (c) A. Kongkanand, N. P. Subramanian, Y. Yu, Z. Liu, H. Igarashi and D. A. Muller, *ACS Catal.*, 2016, **6**, 1578.

2 (a) J.-H. Wee, *Renew. Sust. Energ. Rev.*, 2007, **11**, 1720; (b) A. Rodríguez-Castellanos, J. L. Díaz-Bernabé, S. Citalán-Cigarroa and O. Solorza-Feria, in *Portable hydrogen energy systems. Fuel cells and storage fundamentals and applications*, ed. P. Ferreira-Aparacio and A. M. Chaparro, Elsevier, United Kingdom, 2018, pp. 91-106.

3 F. A. de Bruijn and G. J. M. Janssen, in *Fuel Cells*, ed. K.-D. Kreuer, Springer, New York, 2013, pp. 249-303.

4 S. J. Hamrock and A. M. Herring, in *Fuel Cells*, ed. K.-D. Kreuer, Springer, New York, 2013, pp. 577-605.

5 (a) W. J. Phang, W. R. Lee, K. Yoo, D. W. Ryu, B. Kim and C. S. Hong, *Angew. Chem. Int. Ed.*, 2014, **53**, 8383; (b) P. Ramaswamy, N. E. Wong and G. K. H. Shimizu, *Chem. Soc. Rev.*, 2014, **43**, 5913; (c) Q. Tang, Y. Liu, S. Liu, D. He, J. Miao, X. Wang, G. Yang, Z. Shi and Z. Zheng, *J. Am. Chem. Soc.*, 2014, **136**, 12444; (d) S. Sanda, S. Biswas and S. Konar, *Inorg. Chem.*, 2015, **54**, 1218; (e) J. Liu, X. Zou, C. Liu, K. Cai, N. Zhao, W. Zheng and G. Zhu, *CrystEngComm*, 2016, **18**, 525; (f) S. Chandra, T. Kundu, K. Dey, M. Addicoat, T. Heine and R. Banerjee, *Chem. Mater.*, 2016, **28**, 1489; (g) H.-B. Luo, Q. Ren, P. Wang, J. Zhang, L. Wang and X.-M. Ren, *ACS Appl. Mater. Interfaces*, 2019, **11**, 9; (h) S. Pili, P. Rought, D. I. Kolokolov, L. Lin, I. da Silva, Y. Cheng, C. Marsh, I. P. Silverwood, V. G. Sakai, M. Li, J. J. Titman, L. Knight, L. L. Daemen, A. J. Ramirez-Cuesta, C. C. Tang, A. G. Stepanov, S. Yang and M. Schröder, *Chem. Mater.*, 2018, **30**, 7593.

6 (a) J. Kim, S. Sengodan, G. Kwon, D. Ding, J. Shin, M. Liu and G. Kim, *ChemSusChem*, 2014, **7**, 2811; (b) T. S. Bjørheim, S. M. H. Rahman, S. G. Eriksson, C. S. Knee and R. Haugsrud, *Inorg. Chem.*, 2015, **54**, 2858; (c) K. Singh, R. Kannan and V. Thangadurai, *Int. J. Hydrogen Energy*, 2016, **41**, 13227.

7 (a) M. Sharifi, M. Wark, D. Freude and J. Haase, *Microporous Mesoporous Mater.*, 2012, **156**, 80; (b) J. Zeng, B. He, K. Lamb, R. De Marco, P. K. Shen and S. P. Jiang, *Chem. Commun.*, 2013, **49**, 4655; (c) S. P. Jiang, *J. Mater. Chem. A*, 2014, **2**, 7637; (d) J. Zhang, S. Lu, H. Zhu, K. Chen, Y. Xiang, J. Liu, M. Forsyth and S. P. Jiang, *RSC Adv.*, 2016, **6**, 86575.

8 A. Kumar, W. Pisula, C. Sieber, M. Klapper and K. Müllen, *J. Mater. Chem. A*, 2018, **6**, 6074.

9 (a) D. Basak, S. Christensen, S. K. Surampudi, C. Versek, D. T. Toscano, M. T. Tuominen, R. C. Hayward and D. Venkataraman, *Chem. Commun.*, 2011, **47**, 5566; (b) S. Tan, C. Wang and Y. Wu, *J. Mater. Chem. A*, 2013, **1**, 1022; (c) T. Liang, Y. Wu, S. Tan, X. Yang and B. Wei, *Chem. Phys. Lett.*, 2015, **637**, 22; (d) P.-L. Champagne, D. Ester, D. Polan, V. E. Williams, V. Thangadurai and C.-C- Ling, *J. Am. Chem. Soc.*, 2019, **141**, 9217.

10 S. Tan, B. Wei, T. Liang, X. Yang and Y. Wu, *RSC Adv.*, 2016, **6**, 34038.

11 A. Yildirim, P. Szymoniak, K. Sentker, M. Butschies, A. Bühlmeyer, P. Huber, S. Laschat and A. Schönhals, *Phys. Chem. Chem. Phys.*, 2018, **20**, 5626.

12 J. Sakuda, M. Yoshio, T. Ichikawa, H. Ohno and T. Kato, *New J. Chem.*, 2015, **39**, 4471.

13 T. Ichikawa, M. Yoshio, S. Taguchi, J. Kagimoto, H. Ohno and T. Kato, *Chem. Sci.*, 2012, **3**, 2001.

14 (a) M. Yoshio, T. Mukai, K. Kanie, M. Yoshizawa, H. Ohno and T. Kato, *Adv. Mater.*, 2002, **14**, 351; (b) N. Noujeim, S. Samsam, L. Eberlin, S. H. Sanon, D. Rochefort and A. R. Schmitzer, *Soft Matter*, 2012, **8**, 10914; (c); S.-C. Luo, S. Sun, A. R. Deorukhkar, J.-T. Lu, A. Bhattacharyya and I. J. B. Lin, *J. Mater. Chem.*, 2011, **21**, 1866; (d) T. Kato, M. Yoshio, T. Ichikawa, B. Soberats, H. Ohno and M. Funahashi, *Nat. Rev. Mater.*, 2017, **2**, 17001; (e) B. Soberats, E. Uchida, M. Yoshio, J. Kagimoto, H. Ohno and T. Kato, *J. Am. Chem. Soc.*, 2014, **136**, 9552.

15 C. Cuerva, J. A. Campo, P. Ovejero, M. R. Torres and M. Cano, *Dalton Trans.*, 2014, **43**, 8849.

16 (a) K. Usha, K. Vijayani and S. Chandrasekhar, *Liq. Cryst.*, 1993, **15**, 575; (b) M. Seredyuk, A. B. Gaspar, V. Ksenofontov, Y. Galyametdinov, M. Verdaguer, F. Villain and P. Gütlich, *Inorg. Chem.*, 2008, **47**, 10232; (c) Y. Abe, Y. Takagi, M. Nakamura, T. Takeuchi, T. Tanase, M. Yokokawa, H. Mukai, T. Megumi, A. Hachisuga and K. Ohta, *Inorg. Chim. Acta*, 2012, **392**, 254; (d) K. Ohta, H. Muroki, A. Takagi, K. Hatada, H. Ema, I. Yamamoto and K. Matsuzaki, *Mol. Cryst. Liq. Cryst.*, 1986, **140**, 131; (e) Y. Abe, H. Akao, Y. Yoshida, H. Takashima, T. Tanase, H. Mukai and K. Ohta, *Inorg. Chim. Acta*, 2006, **359**, 3147; (f) M. Prehm, C. Enders, M. Y. Anzahaee, B. Glettner, U. Baumeister and C. Tschierske, *Chem. Eur. J.*, 2008, **14**, 6352.

17 F. Preishuber-Pflügl and M. Wilkening, *Dalton Trans.*, 2014, **43**, 9901.

18 Q. Hou, K.-L. Yan, R.-H. Fan, Z.-D. Zhang, M. Chen, K. Sun and C.-B. Cheng, *RSC Adv.*, 2015, **5**, 9472.

19 C. Cuerva, J. A. Campo, M. Cano and C. Lodeiro, *Chem. Eur. J.*, 2016, **22**, 10168.

20 G. M. Sheldrick, SHELX97, *Software for Refinement of Crystal Structure*, University of Göttingen, Germany, 1997.

Lamellar columnar liquid-crystalline mesophases as a 2D platform for anhydrous proton conduction

View Article Online
DOI: 10.1039/C9TC03627J

Table of contents entry

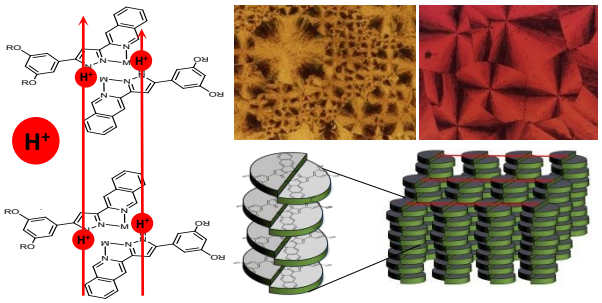

The fluid properties in the mesophase favour the dissociation of the pyrazole proton, and the metallomesogens behave as water-free proton conductors